Teleconnection of the Quasi-biennial oscillation with boreal winter surface climate in Eurasia and North America

Vinay Kumar[1#], Matthew H. Hitchman[2], Wenyuan Du[2], S. K. Dhaka[1], and Shigeo Yoden[3]

[1] Radio and Atmospheric Physics Lab., Rajdhani College, University of Delhi, India

[2] Department of Atmospheric and Oceanic Sciences, University of Wisconsin–Madison, Wisconsin, USA

[3] Institute for Liberal Arts and Sciences, Kyoto University, Kyoto, Japan

#Corresponding author: Vinay Kumar, dabas.vinay@gmail.com

ORCID ID-

Vinay Kumar - https://orcid.org/0000-0003-3582-7625

Matthew H. Hitchman - https://orcid.org/0000-0001-9015-0579

Wenyuan Du - https://orcid.org/0009-0008-7319-4324

S. K. Dhaka - https://orcid.org/0000-0002-0812-525X

Shigeo Yoden - https://orcid.org/0000-0003-1663-4588

Abstract

The present study investigates dynamical coupling between the equatorial stratospheric Quasi-biennial oscillation (QBO) and the boreal winter surface climate of the Northern Hemisphere mid and high latitudes using 42 years data (1979–2020). For neutral El Niño Southern Oscillation (ENSO) periods, QBO westerlies (W) at 70 hPa favor high sea level pressure in the polar region, colder conditions and deeper snow over Eurasia and North America, and the opposite effects for QBO easterlies (E). When QBO anomalies arrive in the upper troposphere and lower stratosphere (UTLS), it is observed that planetary wave activity is enhanced in the extratropical UTLS during QBO W and diminished during QBO E. This QBO teleconnection pathway along the UTLS to the high latitude surface is independent of the "stratospheric pathway" (Holton-Tan mechanism). Diagnosis of this pathway can help to improve understanding of internal sub-seasonal to seasonal variations, and long-range forecasting over Eurasia and North America.

1. Introduction

The role of dynamical coupling between the stratosphere and troposphere and between the tropics and extratropics in causing regional climate variations is a topic of increasing interest. An improved understanding of dynamical coupling at scales from regional to global via tropospheric or stratospheric dynamical mechanisms can be helpful in improving seasonal forecasts for a given region of interest. The boreal winter (December–January–February [DJF]) is a dynamically active season in the Northern Hemisphere (NH), with the presence of vertically propagating planetary wave activity in stratospheric westerlies[1, 2], and more active deep convection in the tropics[3]. In this season, certain kinds of dynamical coupling are possible between the tropical stratosphere and extratropical troposphere. A better understanding of this coupling would benefit the populations of Eurasia and North America with improved winter forecasting, as dynamically modulated by regional and global atmospheric circulations[4, 5]. These include the tropospheric El Niño Southern Oscillation (ENSO)[6], with periodicity ~3–7 years, and the Quasi-biennial oscillation (QBO)[7], which has a periodicity of 22–34 months and is a dominant mode of interannual variability in the equatorial stratosphere.

ENSO is a tropospheric source of dynamical coupling between tropical and extratropical regions, through modulation of planetary waves in both the troposphere and stratosphere[8, 9], and is one of the key ingredients used in forecasting wintertime surface climate anomalies for the NH extratropics[10, 11, 12, 13,14]. ENSO teleconnections can involve both a tropospheric[5] and a stratospheric pathway[13, 15]. Butler et al.[15] reasoned that North America is primarily affected via the tropospheric pathway, involving a shift in the Pacific North America pattern, while the surface climate response over large portions of Eurasia, the Arctic, and the North Atlantic are influenced by the stratospheric pathway via modulation of the polar vortex.

Stratosphere forcing can also contribute to the predictability of climate-related extreme events at the surface[16]. The QBO is a dominant equatorial stratospheric dynamical forcing, having broad impacts over the globe[7]. Its inclusion significantly enhances seasonal to decadal forecast systems[17]. Impacts of the QBO have been studied in the tropical and subtropical region involving the direct effect on deep convective systems[18, 19, 20, 21, 22], and in the polar region via the polar vortex[23, 24 ,25, 26]. The QBO dynamical teleconnection has three potential routes of influence, referred to as the tropical, subtropical, and polar routes[21, 27]. However, these three routes can be classified into two pathways to separate their responses[21, 26, 27, 28]. The tropical and subtropical routes are associated with the "tropospheric pathway" along the tropical and subtropical upper troposphere and lower stratosphere (UTLS)[28]. In this pathway, QBO anomalies in mean meridional circulation (MMC), temperature, and zonal wind[28] can interact with synoptic Rossby wave patterns, which can then affect the extratropical troposphere via modulation of the Northern annular mode (NAM)[23]. The polar route is associated with the "stratospheric pathway", where QBO anomalies of MMC, temperature, and zonal wind in the subtropical stratosphere modulate stratospheric planetary wave absorption (Holton-Tan mechanism or "H-T effect")[29, 30].

Holton and Tan[29, 30] showed that sudden stratospheric warmings (SSWs) occur more often when there are QBO easterlies (E) in the tropical stratosphere near 50 hPa. In turn, SSWs are related to an increase in negative phases of the NAM and Arctic oscillation (AO)[31] in sea-level pressure, and more cold air outbreaks at the surface in North America and Eurasia[31, 32]. The "H-T effect" is an example of the stratospheric pathway from the tropical stratosphere to the extratropical surface. It has also been observed that ENSO modulates the QBO MMC[26, 28], QBO amplitude[33], and QBO period via modulation of its downward propagation speed[33, 34, 35]. Further, both modeling[36] and observational studies[26, 37] have shown that the interaction between different phases of ENSO and

101 the QBO produce a nonlinear effect in the QBO dynamical teleconnection. Hasen et al.[36] showed
102 that QBO anomalies extend down to the troposphere most significantly during La Niña.
103 Observational studies[26, 37] found that La Niña amplifies the QBO dynamical teleconnection to the
104 polar vortex, thereby influencing the stratospheric pathway. Kumar et al.[26] also found that La Niña
105 (El Niño) tends to amplify (nullify) the QBO MMC into the winter hemisphere. Recently, Ma et
106 al.[38] pointed out that QBO teleconnections to the subtropics are more evident during El Niño
107 winters, while teleconnections to the polar regions are more evident during La Niña winters.
108 ENSO influences both the tropospheric and stratospheric pathways. It is therefore important to
109 investigate each combined ENSO and QBO state in order to understand QBO teleconnections.
110 As mentioned above, in past studies, the influence of the QBO on the high latitude boreal winter
111 surface climate was discussed in terms of modulation of polar vortex intensity[27, 39, 40]. However, a
112 complete dynamical mechanism for downward coupling is yet to be established[41]. Until now, QBO
113 winter teleconnections to the surface have been reproduced in models with mixed success, and
114 current QBO forecast biases highlight model deficiencies needing future improvement [42]. Updated
115 observational studies will play a crucial role in such improvements. Most of these studies used a
116 single level for the QBO index, either 30 hPa, 50 hPa, or 70 hPa and considered two phases of the
117 QBO, westerly and easterly irrespective of ENSO phases. However, the QBO varies continuously
118 in phase, with a distinct pattern of temperature and wind anomalies associated with the QBO MMC
119 that descend in time such that any one-point experiences a sinusoidal range of phases (see, e.g.,
120 Fig.1 and 21 of Hitchman et al.[28]). In the present work we define QBO phase using empirical
121 orthogonal function (EOF) analysis, which includes phase information over a wider range of
122 altitudes than a single level index. The method of Wallace et al.[43] is adopted to define QBO phase
123 angle. Here we seek to identify a QBO - surface weather climate linkage using composite

differences between opposite phase angles of the QBO in the most recent European Centre for Medium-Range Weather Forecasts (ECMWF) Reanalysis v5 (ERA-5) data set from of the satellite era 1979 – 2020. As discussed above the role of ENSO is important in determining the boreal winter surface climate as well as influencing QBO dynamical teleconnection. In this work, the joint effects of the ENSO and QBO are discerned in a systematic fashion using a phase sweep of the QBO phase angle. This allows for investigating the effects of different phase combinations of ENSO and the QBO in determining NH winter surface climate.

2. Results

2.1 Zonal mean results

In order to study the influence of the QBO on NH surface weather during DJF, monthly zonal mean anomalies are calculated for (lower stratospheric) 100 hPa geopotential height (GPH′), mean sea level pressure (MSLP′), and surface temperature at 2 m (T′). The single prime superscript indicates de-seasonalized anomalies, the departure from the climatological mean annual cycle in the 42-years data set (see section 4.1). The zonal mean analysis is based on composite differences between the two groups G1 and G2 ($\theta_c \pm \frac{\Delta\theta}{2}$, *and* $\theta_c + 180° \pm \frac{\Delta\theta}{2}$, respectively) of QBO opposite phases, where θ_c is the central phase angle of the group and the averaging angle is $\Delta\theta = 120°$ (see Methods, Fig. 1 b). A phase sweep of QBO central phase angle is performed, changing the phase every 1° in a complete cycle (0°–360°), to search the phase dependency for statistically significant effects. El Niño and La Niña periods were defined by when the Niño 3.4 monthly mean index exceeded ± 0.4 K. These analyses were done separately for All, Neutral, El Niño, and La Niña groupings of monthly means (Fig. 2).

In the All category, significant negative differences of GPH′ anomalies at 100 hPa can be seen in the NH polar region (> 60°N) for the phase angle range $100° < \theta_c < 140°$ (Fig.2a). These significant

patterns are mainly contributed by La Niña (Fig. 2d), which exhibits more significant patterns in a wider phase domain ($70° < \theta_c < 210°$) with strong amplitude, and are absent for the neutral and El Niño periods (Fig. 2b and c). Significant patterns for La Niña are centered around 135° phase angle, which represents a QBO westerly wind maximum at 50 hPa (see, e.g., Fig.3 of Kumar et al.[26]), where 50 hPa QBO W phase coincides with low geopotential height over the pole. This analysis confirms the finding of Kumar et al.[26], that the H-T mechanism is amplified during La Niña. Interestingly for neutral ENSO, all the variables exhibit systematic significant modulations simultaneously in the extratropical and polar regions for a broad phase range ($120° < \theta_c < 240°$) with centroid at 180° (vertical dashed line) (Fig. 2b, f, and j). Note that the composite difference G1 – G2 at centroid angle 180° is representative of QBO W – QBO E phase at 70 hPa and the reverse phase at 20 hPa (Fig. 1c). Significant negative anomalies of GPH′ at 100 hPa in the tropical to extratropical transition region (20°N - 40°N) are associated with positive MSLP′ anomalies in the polar region (> 50°N) and negative T′ at 2 m anomalies in the high latitude region (50°N - 70°N). The significant anomalies in surface temperature extend up to 500 hPa (not shown).

These results suggest that it would be useful to explore the phase combination of neutral ENSO and centroid QBO phase angle 180° to better understand the joint QBO/ENSO influence on the NH high latitude surface via the tropical\extratropical UTLS. Figures 2g, h, k, and l show that El Niño and La Niña interact with the QBO in a complex way to influence surface weather climate in the extratropical and polar regions. Considerations for interpretation include the modest sample size, uneven distribution of El Niño and La Niña events for QBO phases G1 and G2, and uneven distribution of strong El Niño or La Niña events in the particular QBO phase bins. It is also possible that there are significant longitudinal variations for a particular ENSO/QBO phase combination, but the zonal mean structure is not significantly modulated.

The present analysis focuses on neutral ENSO only at centroid angle 180°, for which G1 contains 10 months from 5 different winters and G2 contains 16 months from 8 different winters. Using one month as a basic unit, and using a low threshold value (± 0.4 K) for evaluating ENSO neutral, help to minimize ENSO bias for a particular phase of the QBO (G1 or G2).

2.2 Zonally asymmetric results for neutral ENSO

This analysis is extended for non-zonal components to explore the regional dependency of QBO modulation. Results are shown in NH polar orthographic projection in Fig. 3, for central phase angle $\boldsymbol{\theta_c}$ = 180° during DJF and neutral ENSO. Top to bottom rows show 100 hPa GPH, MSLP, T at 2 m, and snow depth, respectively. The 1st column represents the 42-year DJF mean for neutral ENSO, while the 2nd to 4th columns show composites of G1 anomalies, G2 anomalies, and their composite difference G1– G2, respectively.

During QBO W (G1, Fig. 3, 2nd column) a 100 hPa ridge is amplified over the Bering Sea, near the base of the climatological Aleutian High[44], MSLP is higher over the Arctic, and the midlatitude continents are colder and snowier. During QBO E (G2, Fig. 3, 3rd column) there is a somewhat different wave two anomaly pattern, with low 100 hPa heights over the Bering Sea, reduced MSLP over the Arctic, and the midlatitude continents are warmer and less snowy. The composite difference G1– G2 of GPH′ anomalies at 100 hPa shows a nearly wavenumber 2 pattern in the extratropical region (30°N – 60°N) with significant negative anomalies across North America and southwestern Europe, and (statistically insignificant) over Northern Russia (Fig. 3a, 4th column). The wavenumber 2 feature is present from 100 hPa to the boundary layer; and below the 100 hPa level the Northern Russia pattern becomes statistically significant. A significant positive anomaly in 100 hPa GPH′ lies over the Bering Sea. These results are consistent with excitation of a weak NAM and more cold air outbreaks over the continents[28, 32] during QBO W and neutral ENSO.

These composite difference patterns exhibit minor nonlinear features between G1 and G2, with stronger amplitude and a wider region for group G1. We hypothesize that the wavenumber 2 pattern may have been induced by the tropospheric pathway of QBO influence along the UTLS. In this connection, a significant positive pattern can be seen in MLSP′ as a semi-disc structure (150°W-60°E) from 60°N to the north pole, including North America, Greenland, Iceland, northern Europe, and the Norwegian Sea (Fig. 3b, 4th column). Significant negative patterns over southern Europe extend across the Mediterranean Sea and North Africa to the equator.

More robust features are seen in T′ at 2 m anomalies, with significant negative patterns over the Eurasian and North American sectors (Fig. 3c, 4th column), and simultaneously significant positive patterns spread across the northern Arabian Peninsula, part of eastern North Africa, and the Mediterranean Sea. Weakly significant positive patterns can also be observed near the Aleutian and Icelandic low-pressure systems. Similar patterns are found for snow depth anomaly over the both Eurasian and North American sectors, but with the opposite sign and smaller-scale features. Snow depth is higher when it is colder. The patterns of MLSP′, T′ at 2 m, and snow depth exhibit a linear transition from G1 to G2 with a marginally stronger amplitude for G1.

2.3 Regional dependence on QBO phase angle for neutral ENSO

In order to further investigate particular regions of interest, we analyzed the series for MSLP′and T′ at 2 m against QBO phase angle over selected domains which exhibited significant patterns for DJF during neutral ENSO (Fig. 3). The area of interest for MSLP′ is the significant region in the composite difference highlighted by the back dots over the positive golden color at the polar region, and over the negative dark green color at southwestern Europe (Fig. 3b, 4th column), and for T′ at 2 m the significant region of black dots over the negative dark green color at Eurasia, and North America (Fig. 3c, 4th column). A sine trigonometric function with mean amplitude defined

from both groups (G1 and G2) is applied to each series. All resulting series with QBO phase are shown in Fig. 4, reflecting sinusoidal waves with phase constant 90° (dashed line).

As expected, the MSLP′ series over the Arctic and southwestern Europe have a phase difference of 180° because their significant patterns show the opposite sign for composite differences (Fig. 2b, 4th column). The composite difference for MSLP between G1 and G2 is greater than 6 hPa (3 hPa) for the Arctic (southwestern Europe), and that for T′ at 2 m is greater than 2 K (4 K) for Eurasia (North America). The statistical significance of each difference series exceeds 99% for groups G1 and G2. Since the sampling is limited, we also used a bootstrap method with 10,000 resampling members to estimate the significance of G1 and G2. Results are shown in the adjacent histogram plots on the right-hand side of each series. The first histogram corresponds to non-parametric bootstrapping on the ratio of variance (f-test) for G1 and G2, and the second corresponds to bootstrapping on the difference of the means for G1 and G2. The yellow vertical line represents the original ratio of variance and difference of mean for G1 and G2 in the first and second histograms, respectively. The regions between the two red vertical lines lie at a 99% significant level. The significance is also met for the bootstrapping. The sinusoidal characteristics in the original sampling with QBO phase angle and the significance level in bootstrapping reflect the robustness of the results. These significant composite differences of MSLP′ and T′ at 2 m between the opposite QBO phases contain meaningful applications for seasonal and longer time-scale forecasts, although internal variations within each group are not also small.

3. Discussion

After confirming a consistent result with our previous study[26] that the H-T mechanism is amplified during the La Niña period, the present study investigates the QBO teleconnection with the boreal winter surface climate of NH mid and high latitudes regions in the presence and absence of El Niño and La Niña effects. A significant modulation of the climate dynamics governing surface

anomalies is observed in the zonal mean and zonally asymmetric quantities for a specific QBO phase at the centroid angle of 180° for neutral ENSO period only (– 0.4 K < Niño 3.4 index < – 0.4K). This specific QBO phase group G1 corresponds to maximum westerly wind at 70 hPa (QBO W) and simultaneously opposite easterly maximum at 20 hPa, whereas G2 group (QBO E) has the opposite signs.

The QBO modulations of surface temperature and snow depth in Eurasia and North America illustrates a systematic association with MSLP in the arctic region. High pressure conditions over the polar region induce colder temperatures over the midlatitude continents and vice-versa. It is observed that ENSO neutral and QBO W favors a high value of MSLP (> 6 hPa) over the polar region (>50°N), and cold conditions (~ 2 – 4K) with high snow depth over Eurasia and North America, and the opposite effects during QBO E. A comparison of the anomaly patterns for QBO W and QBO E shows that the response is fairly linear, with marginally stronger amplitude for QBO W. During QBO W, anticyclonic anomalies are found at 100 hPa over the Bering Sea and the high North Atlantic. This favors higher arctic MSLP, especially in the North Atlantic. The pattern of colder surface temperatures extends farther into the midlatitudes, with enhanced snowfall farther south than normal, favoring a low index NAM [23] and negative AO[31]. During QBO E, the Aleutian High and the trough over eastern North America at 100hPa are reduced in amplitude such that the polar vortex is more zonally symmetric, with a region of lower MSLP over the pole. Such a high index NAM/AO flow confines polar air to higher latitudes, giving a warm anomaly across Eurasia and North American and reduced snow depth.

These results suggest that tropospheric wave activity is enhanced at high latitudes during QBO W and diminished during QBO E for the neutral ENSO period. This QBO pathway to the high latitude surface is independent of the traditional “stratospheric pathway” or H-T mechanism. To explore

263 the hypothesis that there is enhanced planetary wave activity in the extratropical troposphere
264 during QBO W for the neutral ENSO period, we investigate the joint effect of the QBO and ENSO
265 on the Eliassen-Palm (EP) flux and flux divergence, which is shown in Fig. 5. In the DJF
266 climatology there are two branches of EP fluxes, with some wave activity propagating upward in
267 the troposphere near 40°N and refracting equatorward along the UTLS (Fig. 5, left column), and
268 another branch propagating upward in the stratosphere near 60°N. A region of poleward flux of
269 wave activity can also be observed along the UTLS from equator to 15°N. It is difficult to discern
270 any differences among the phases on ENSO in the climatology plots, although there are some
271 differences in the shape of the zero-wind line of the zonal mean zonal wind in the lower
272 stratosphere (Figs. 5a-c, left column). In the climatology one may also observe the vertical dipole
273 of divergence/convergence of the EP flux (i.e., westerly/easterly wave drag) in the extratropical
274 troposphere due to the baroclinic disturbances**.**

275 During QBO W and neutral ENSO the equatorward refraction of Rossby wave activity along the
276 UTLS in the subtropics is diminished and the upward branch in the extratropical stratosphere is
277 enhanced (Fig. 5a, G1), consistent with poleward confinement of wave activity and a higher
278 amplitude wave two pattern in the lower stratosphere (Fig. 3a, G1). During QBO E, the
279 equatorward branch along the UTLS is stronger and the upward branch in the extratropical
280 stratosphere is diminished (Fig. 5a, G2). This pattern is more noticeable in their difference (Fig.
281 5a, G1-G2). These results are consistent with the high index NAM/AO patterns during QBO E and
282 neutral ENSO shown in Fig.3.

283 In order to see the QBO route though the subtropical jets (STJs), the joint effect of the QBO and
284 ENSO on the STJ is shown in Fig. 6. During neutral ENSO months (Fig. 6a), the amplified
285 Aleutian High at 100 hPa during QBO W implies reduced westerlies across the Pacific and an

equatorward shift in the STJ (Fig. 6a, G1), but in the Atlantic sector, an amplified Icelandic Low coincides with a stronger, northward-shifted STJ across the Mediterranean Sea. During QBO E and neutral ENSO (Fig. 6a, G2) the Pacific STJ is strengthened and zonal winds in the North Atlantic are stronger, consistent with a higher index NAM flow. During El Niño, the anomalies in G1 and G2 are diminished, but with similar difference patterns to neutral ENSO in the Atlantic and Eurasia (Figure 6b), whereas QBO modulation is weak over the Pacific. During La Niña, the anomaly fields in G1, G2 and their difference show similar patterns to neutral ENSO, but with opposite sign and weaker amplitudes.

The joint effects of the QBO and ENSO on zonally asymmetric features of wind speed in the upper troposphere (Figure 6) are consistent with the anomalies of E-P flux and its divergence (Figure 5). These results suggest that, for neutral ENSO, when QBO anomalies of MMC, temperature and zonal wind arrive in the UTLS, there is a QBO tropospheric pathway of influence via the subtropical UTLS towards to high latitudes surface through wave mean flow interaction[20], instead of through modulation of the polar vortex via the stratospheric pathway (H-T effect). In discussing possible mechanisms by which the QBO can influence the STJs, Wang et al.[45] included changes in baroclinicity, eddy refraction, and changes in tropopause height. Although not yet fully understood, through the interaction among QBO anomalies, synoptic waves, and planetary waves, the tropospheric wave pattern is enhanced at high latitudes during QBO W, and is diminished during QBO E for neutral ENSO. This QBO teleconnection pathway through the STJs to the high latitude surface is independent of the traditional "stratospheric pathway" or H-T mechanism. Diagnosis of this pathway will provide valuable input to global circulation model simulations of internal sub-seasonal to seasonal variations, and can be implemented to improve long-range forecasting of these time scales over the Eurasian and North American areas.

4. Data and Method

4.1 Data

ERA-5 reanalysis monthly mean data for the 42 years period 1979 to 2020 are used to analyze MSLP, T at 2 m, snow depth, horizontal winds (U, V), and geopotential height (GPH). The data are available at 37 pressure levels from 1000 hPa to 1 hPa. Due to development in model physics, core dynamics, and data assimilation, the ERA-5 data set offers several improvements over its predecessor (ERA-Interim)[46]. ERA-5 allows for the detailed evolution of weather systems as it outperforms the high-resolution regional analysis with a 31-km horizontal resolution[46]. ENSO phase is defined based on the Niño 3.4 index in monthly mean data. The Hadley Centre Global Sea Ice and Sea Surface Temperature (HadISST) v1.1 data [47] is used to calculate the monthly Niño 3.4 index, which is defined as the de-seasonalized SST anomaly for the 42-year data set in the pacific region 5°N–5°S, 120°W–170°W. Any month during the 42 years is considered to be during El Niño or La Niña whenever the Niño 3.4 index exceeds the threshold values ± 0.4 K (+ El Niño, – La Niña). All of the zonal and non-zonal analyses are performed at 2.5° spatial grid resolution.

4.2 Methods

4.2.1 QBO phase angle:

The method of Wallace et al.[43] is used to represent the QBO in empirical orthogonal function (EOF) phase space for equatorial zonal mean zonal wind varying in altitude and time. The EOFs are obtained from the covariance matrix of the de-seasonalized stratospheric zonal mean zonal wind (U') in the equatorial region at the five pressure levels 70, 50, 30, 20, and 10 hPa. The vertical structure of the first two leading EOFs is shown in Fig. 1a. These two functions explain 94.72% (58.07% plus 36.65%) of the total variance. EOF1 reflects the opposite phase of zonal wind in the upper (< 50 hPa, positive) and lower (> 50 hPa, negative) stratosphere, while EOF2 reflects maximum zonal wind in the mid-stratosphere (around 30 hPa, positive). A scatter plot of the first

two principal components (*PC*1 and *PC*2) associated with these two EOFs is shown in Fig. 1b (for DJF only). The QBO phase angle is defined as $\theta = tan^{-1}\frac{PC2_c}{PC1_c}$, where $PC1_c$ and $PC2_c$ are defined with respect to the locus of the centroid (Cx, Cy) of all months for 42 years (shown as a + green marker in Fig. 1b) i.e., $PC1_c = PC1 - Cx$, and $PC2_c = PC2 - Cy$. The centroid is determined numerically (2.22, – 4.79) to minimize the variance of the distance to all points for the whole data period. Successive progression of the QBO-phase angle $\boldsymbol{\theta}$ can be seen with time (Fig. 1d) except for the disturbed periods 2015/2016 and 2019/2020. As introduced by Kumar et al.[26], this study uses the same composite difference analysis for a central angle $\boldsymbol{\theta_c}$ between two groups G1 and G2 of QBO opposite phases ($\theta_c \pm \frac{\Delta\theta}{2}, and\ \theta_c + 180° \pm \frac{\Delta\theta}{2}, respectively$, $\Delta\theta = 120°$), and also gives weight to the phase transition between these two opposite groups (i.e., 60° between G1 and G2 and 60° between G2 and G1). Therefore, the composite difference analysis will neglect the phase transition between two opposite phases of the QBO. As an example, G1 and G2 are shown, along with a dashed line at the central angle θ_c = 180° (Fig.1 b). Most results are shown for groups G1 and G2 with central angle θ_c = 180° (Fig. 1b, c), for which G1 corresponds to QBO W phase at 50 to 70 hPa, and G2 corresponds to QBO E phase at 50 to 70 hPa with clear separation between these two phases at 70hPa, and simultaneously the opposite phase at 20 hPa (Fig. 1c). Using individual months, the statistical significance of the composite difference is evaluated using a two-sided Student's *t*-test, assuming two independent samples in each G1 and G2 group. All results for composite difference patterns are discussed at the 95% significant level. Further, to avoid monthly intra-seasonal variability within a group, deseasonalized anomalies are used for the composite difference analysis. A single superscript prime on any variable, X′, represents the de-seasonalized anomaly, i.e., its deviation from the 42 year (1979-2020) climatological mean annual cycle.

356 **4.2.2 EP flux and divergence:**

357 The EP flux[48] is a diagnostic tool for assessing wave propagation and wave-mean flow interaction.
358 It is a vector representation for the propagation of synoptic and planetary Rossby wave activity in
359 the meridional plane. An upward component indicates a poleward heat flux while an equatorward
360 component indicates a poleward momentum flux. EP flux divergence implies a source of Rossby
361 wave activity, and EP flux convergence implies absorption of Rossby wave activity. EP flux
362 divergence represents the body force, or net effect of waves on the zonal mean zonal wind, with
363 EP flux convergence causing deceleration of zonal mean westerlies and EP flux divergence causing
364 acceleration. The primary effect of a region of EP flux convergence, however, is to induce
365 poleward motion, with an associated MMC and quadrupole of temperature anomalies in the
366 meridional plane (warm over cold in the tropics and cold over warm at high latitudes) associated
367 with adiabatic vertical motions.

368 The meridional and vertical components of the EP flux are calculated in pressure coordinates using
369 the following expressions[49, 50]:

370 $\mathrm{f_\phi} = -\overline{\mathrm{u'\,v'}} + \overline{\mathrm{u_p}}\frac{\overline{\mathrm{u'\,\theta'}}}{\overline{\theta_p}}$, $\mathrm{f_p} = \left(\mathrm{f} - \frac{1}{\mathrm{a}\cos\phi}\frac{\partial(\bar{\mathrm{u}}\cos\phi)}{\partial\phi}\right)\frac{\overline{\mathrm{v'\,\theta'}}}{\overline{\theta_p}} - \overline{\mathrm{u'\,w'}}$, and

371 $\mathrm{F} = \left(\mathrm{F_\phi}, \mathrm{F_p}\right) = \rho\,\mathrm{a}\cos\phi\,(\mathrm{f_\phi}, \mathrm{f_p})$, where

372 ϕ is latitude, p pressure, u zonal wind, v meridional wind, w vertical wind, θ potential
373 temperature, $f = 2\,\Omega\sin\phi$ is the Coriolis parameter, Ω is the angular frequency of Earth's
374 rotation, a denotes the Earth's radius, and $\rho\ (p)$ is mean density. The zonal mean is indicated with
375 an overbar; a prime denotes a departure from the zonal mean. Potential temperature is calculated
376 from $\theta = T\left(\frac{P_0}{P}\right)^{\kappa}$ and density from $\rho = \rho_0\frac{P}{P_0}$. The EP flux divergence is calculated from $\vec{\nabla}\cdot\vec{F} =$
377 $\frac{1}{\rho\,a\cos\phi}\frac{\partial(\cos\phi F_\phi)}{\partial\phi} + \frac{1}{\rho\,a\cos\phi}\frac{\partial(F_p)}{\partial p}$. Twice daily (0000 and 1200 UTC) ERA-5 analyses are used

for calculating EP fluxes and then monthly mean averages are constructed. EP flux arrows are scaled by $\sqrt{p_o/p}$ in order to see features in the upper stratosphere.

Acknowledgments: The authors would like to thank all members of the ERA-5 reanalysis, and HadISST teams for providing the data sets. MHH was supported by NSF grant AGS 1947658.

Competing Interests: The authors declare that there are no competing interests.

Author Contributions: VK and SY jointly worked on the research design and methodology. VK analyzed the data and wrote the first draft of the paper. MHH and WD jointly performed the analysis for EP flux. MHH contributed significantly in the discussion section. MHH, WD, SKD, and SY contributed to the conceptualization, review, and edited the draft.

Data availability statement: All data used in this study are openly accessible for the public. The ERA-5 data set is available online at https://cds.climate.copernicus.eu/cdsapp#!/home. The HadISST data set is available at https://www.metoffice.gov.uk/hadobs/hadisst/data/download.html. The EP fluxes data are archived in Zenodo (https://doi.org/10.5281/zenodo.10140775 [51])

Code availability statement: All programming codes to generate the figures in this paper are available with the corresponding author, Vinay Kumar, and can be provided on request.

References

1. Charney, J.G. & Drazin, P.G. Propagation of planetary-scale disturbances from the lower into the upper atmosphere. *J. Geophys. Res.* **66**, 83–109 (1961). https://doi.org/10.1029/JZ066i001p00083
2. Andrews, D.G. Wave, mean-flow interaction in the middle atmosphere. *Adv. Geophys.* **28A**, 249–275 (1985). https://doi.org/10.1016/S0065-2687(08)60226-5
3. Liebmann, B. & Hartmann, D.L. Interannual variations of outgoing IR associated with tropical circulation changes during 1974-78. *J. Atmos. Sci.* **39**, 1153-1162 (1982). https://doi.org/10.1175/1520-0469(1982)039<1153:IVOOIA>2.0.CO;2
4. Linkin, M.E. & Nigam, S. The North Pacific Oscillation–West Pacific teleconnection pat-tern: Mature-phase structure and winter impacts. *J. Clim.* **21(9)**, 1979– 1997 (2008). https://doi.org/10.1175/2007JCLI2048.1
5. Budikova, D., Ford, T.W. & Wright, J.D. Characterizing winter season severity in the Mid-west United States, part II: interannual variability. *Int. J. Climatol.* **42**, 3499– 3516 (2022). https://doi.org/10.1002/joc.7429

6. Trenberth, K.E. The definition of El Niño. *Bull. Am. Meteorol. Soc.* **78(12)**, 2771–2778 (1997). https://doi.org/10.1175/1520-0477(1997)078<2771:TDOENO>2.0.CO;2
7. Baldwin, M.P., Gray, L.J., Dunkerton, T.J., Hamilton, K., Haynes, P.H., Randel, W.J., Holton, J.R., Alexander, M.J., Hirota, I., Horinouchi, T., Jones, D.B.A., Kinnersley, J.S., Marquardt, C., Sato, K. & Takahashi, M. The quasi-biennial oscillation. *Rev. Geophys.* **39**, 179-229 (2001). https://doi.org /10.1029/1999RG000073
8. Horel, J.D. & Wallace, J.M. Planetary-scale atmospheric phenomena associated with the southern oscillation. *Mon. Weather Rev.* **109(4)**, 813–829 (1981). https://doi.org/10.1175/1520-0493(1981)109<0813:PSAPAW>2.0.CO;2
9. van Loon, H. & Labitzke, K. The Southern Oscillation Part V: The anomalies in the lower stratosphere of the Northern Hemisphere in winter and a comparison with the quasi-biennial oscillation. *Mon. Weather Rev.* **115(2)**, 357–369 (1987). https://doi.org/10.1175/1520-0493(1987)115<0357:TSOPVT>2.0.CO;2
10. Ropelewski, C.F. & Halpert, M.S. North American precipitation and temperature patterns associated with the El Niño/Southern Oscillation (ENSO). *Mon. Weather Rev.* **114**, 2352–62 (1986). https://doi.org/10.1175/1520-0493(1986)114<2352:NAPATP>2.0.CO;2
11. Higgins, R.W., Leetmaa, A. & Kousky, V.E. Relationships between climate variability and winter temperature extremes in the United States. *J. Clim.* **15(3)**, 1555–1572 (2002). https://doi.org/10.1175/1520-0442(2002)015<1555:RBCVAW>2.0.CO;2
12. Lee, S., Park, H.S., Song, S.Y. & Yeh, S.W. Distinct impacts of two types of El Niño events on northern winter high-latitude temperatures simulated by CMIP6 climate models. *Environ. Res. Lett.* **18(3)**, 034035 (2023). https://doi.org/10.1088/1748-9326/acbce9
13. Ineson, S. & Scaife, A. The role of the stratosphere in the European climate response to El Niño. *Nature Geosci.* **2**, 32–6 (2009). https://doi.org/10.1038/ngeo381
14. Luo, B.H., Luo, D.H., Dai, A.G., Simmonds, I. & Wu, L. A connection of winter Eurasian cold anomaly to the modulation of Ural blocking by ENSO. *Geophys. Res. Lett.* **48,** e2021GL094304 (2021). https://doi.org/10.1029/2021GL094304.
15. Butler, A.H., Polvani, L.M. & Deser, C. Separating the stratospheric and tropospheric pathways of El Niño Southern Oscillation teleconnections. *Environ. Res Lett.* **9**, 024014 (2014). https://doi.org/10.1088/1748-9326/9/2/024014

16. Domeisen, D.I.V., & Butler, A.H. Stratospheric drivers of extreme events at the Earth's surface. *Commun Earth Environ* **1**, 59 (2020). https://doi.org/10.1038/s43247-020-00060-z
17. Scaife, A. A. & et al. Predictability of the Quasi-Biennial Oscillation and its northern winter teleconnection on seasonal to decadal timescales. *Geophys. Res. Letts.*, **41**, 1752–1758 (2014). https://doi.org/10.1002/2013GL059160
18. Gray, W.M., Scheaffer, J.D. & Knaff, J.A. Influence of the stratospheric QBO on ENSO variability. *J. Meteorol. Soc. Jpn.* **70(5)**, 975–995 (1992). https://doi.org/10.2151/jmsj1965.70.5_975
19. Collimore, C.C., Martin, D.W., Hitchman, M.H., Huesmann, A. & Waliser, D.E. On the relationship between the QBO and tropical deep convection. *J. Clim.* **16**, 2552–2568.975 (2003). https://doi.org/10.1175/1520-0442(2003)016%3C2552:OTRBTQ%3E2.0.CO;2
20. Garfinkel, C.I. & Hartmann, D.L. The influence of the quasi-biennial oscillation on the troposphere in winter in a hierarchy of models. Part I: Simplified Dry GCMs. *J. Atmos. Sci.* **68(6)**, 1273–1289 (2011). https://doi.org/10.1175/2011JAS3665.1
21. Haynes, P., Hitchcock, P., Hitchman, M., Yoden, S., Hendon, H., Kiladis, G., Kodera, K. & Simpson, I. The influence of the stratosphere on the tropical troposphere. *J. Meteorol. Soc. Jpn.* **99(4)**, 803–845 (2021). https://doi.org/10.2151/jmsj.2021-040.
22. Yoden, S., Kumar, V., Dhaka, S.K. & Hitchman, M.H. Global monsoon systems and their modulation by the equatorial Quasi-Biennial Oscillation. *MAUSAM* **74(2)**, 239–252 (2023). https://doi.org/10.54302/mausam.v74i2.5948
23. Thompson, D.W.J. & Wallace, J.M. Annular modes in the extratropical circulation Part I. Month-to-month variability. *J. Clim.* **13(5)**, 1000–1016 (2000). https://doi.org/10.1175/1520-0442(2000)013<1000:AMITEC>2.0.CO;2
24. Garfinkel, C.I. & Hartmann, D.L. Different ENSO teleconnections and their effects on the stratospheric polar vortex. *J. Geophys. Res.* **113(D18)**, D18114 (2008). https://doi.org/10.1029/2008JD009920
25. Hu, J., Li, T., Xu, H. & Yang, S. Lessened response of boreal winter stratospheric polar vortex to El Niño in recent decades. *Clim. Dyn.* **49(1-2)**, 263–278 (2017). https://doi.org/10.1007/s00382-016-3340-z

26. Kumar, V., Yoden, S. & Hitchman, M.H. QBO and ENSO effects on the mean meridional circulation, polar vortex, subtropical westerly jets, and wave patterns during boreal winter. *J. Geophys. Res. Atmos.* **127**, e2022JD036691 (2022). https://doi.org/10.1029/2022JD036691
27. Gray, L.J., Anstey, J.A., Kawatani, Y., Lu, H., Osprey, S. & Schenzinger, V. Surface impacts of the Quasi Biennial Oscillation. *Atmos. Chem. Phys.* **18**, 8227–8247 (2018). https://doi.org/10.5194/acp-18-8227-2018
28. Hitchman, M.H., Yoden, S., Haynes, P.H., Kumar, V. & Tegtmeier, S. An observational history of the direct influence of the stratospheric Quasi-Biennial Oscillation on the tropical and subtropical upper troposphere and lower stratosphere. *J. Meteorol. Soc. Jpn.* **99** (2), 239-267 (2021). https://doi.org/10.2151/jmsj.2021-012
29. Holton, J.R. & Tan, H.-C. The influence of the equatorial quasi-biennial oscillation on the global circulation at 50 mb. *J. Atmos. Sci.* ***37*****(10)**, 2200–2208 (1980). https://doi.org/10.1175/1520-0469(1980)037<2200:TIOTEQ>2.0.CO;2
30. Holton, J.R. & Tan, H.-C. The quasi-biennial oscillation in the Northern Hemisphere lower stratosphere. *J. Meteorol. Soc. Jpn.* **60(1)**, 140–147 (1982). https://doi.org/10.2151/jmsj1965.60.1_140
31. Thompson, D.W.J. & Wallace J.M. The Arctic oscillation signature in the wintertime geopotential height and temperature fields. *Geophys. Res. Lett.* **25(9)**,1297–1300 (1998). https://doi.org/10.1029/98GL00950
32. Thompson, D.W.J., Baldwin, M.P. & Wallace J. M. Stratospheric connection to Northern Hemisphere wintertime weather: Implications for prediction. *J. Clim.* **15(12)**, 1421–1428(2002). https://doi.org/10.1175/1520-0442(2002)015<1421:SCTNHW>2.0.CO;2
33. Taguchi, M. Observed connection of the stratospheric quasi biennial oscillation with El Nino-Southern Oscillation in radiosonde data. *Journal of Geophysical Research*, **115(D18)**, D18120 (2010). https://doi.org/10.1029/2010JD014325
34. Yuan, W., Geller, M. A., & Love, P. T. ENSO influence on QBO modulations of the tropical tropopause. *Q. J. Roy. Meteorol. Soc.*, **140**, 1670–1676 (2014). https://doi.org/10.1002/qj.2247

35. Zhou, T., DallaSanta, K. J., Orbe, C., Rind, D. H., Jonas, J. A., Nazarenko, L., Schmidt, G. A., & Russell, G. Exploring the ENSO modulation of the QBO periods with GISS E2.2 models. *Atmos. Chem. Phys.*, **24**, 509–532 (2024).https://doi.org/10.5194/acp-24-509-2024
36. Hansen, F., Matthes, K., & Wahl, S. Tropospheric QBO–ENSO interactions and differences between the Atlantic and Pacific. *Journal of Climate*, **29**, 1353–1368 (2016). https://doi.org/10.1175/JCLI-D-15-0164.1
37. Wei, K., Chen, W., & Huang, R. Association of tropical Pacific sea surface temperatures with the stratospheric Holton-Tan oscillation in the Northern Hemisphere winter. *Geo. Res. Let.s*, **34(16)**, L16814 (2007). https://doi.org/10.1029/2007GL030478
38. Ma, T., Chen, W., An, X., Garfinkel, C. I., & Cai, Q. Nonlinear effects of the stratospheric Quasi-Biennial Oscillation and ENSO on the North Atlantic winter atmospheric circulation. *Journal of Geo. Res. Atmospheres*, **128**, e2023JD039537 (2023). https://doi.org/10.1029/2023JD039537
39. Kidston, J., Scaife, A., Hardiman, S. *et al.* Stratospheric influence on tropospheric jet streams, storm tracks and surface weather. *Nature Geosci* **8**, 433–440 (2015). https://doi.org/10.1038/ngeo2424
40. Cai, Q., Chen, W., Chen, S., Ma, T. & Garfinkel, C.I. Influence of the Quasi-Biennial Oscillation on the spatial structure of the wintertime Arctic Oscillation. *J. Geophys. Res. Atmos.* **127**, e2021JD035564 (2022). https://doi.org/10.1029/2021JD035564
41. Butchart, N. The stratosphere: a review of the dynamics and variability. *Weather Clim. Dynam.*, **3**, 1237–1272 (2022). https://doi.org/10.5194/wcd-3-1237-2022
42. Anstey, J.A., Osprey, S.M., Alexander, J. & *et al.* Impacts, processes and projections of the quasi-biennial oscillation. *Nat Rev Earth Environ,* **3**, 588–603 (2022). https://doi.org/10.1038/s43017-022-00323-7
43. Wallace, J.M., Panetta, R.L. & Estberg, J. Representation of the equatorial stratospheric Quasi-Biennial Oscillation in EOF phase space. *J. Atmos. Sci.* **50(12)**, 1751–1762 (1993). https://doi.org/10.1175/1520-0469(1993)050<1751:ROTESQ>2.0.CO;2
44. Harvey, V. L., & Hitchman, M. H. A climatology of the Aleutian High. *J. Atmos. Sci.*, **53**, 2088-2101 (1996). https://doi.org/10.1175/1520-0469(1996)053<2088:ACOTAH>2.0.CO;2

45. Wang, J., Kim, H.-M., & Chang, E. K. M. Interannual modulation of Northern Hemisphere winter storm tracks by the QBO. *Geo. Res. Lett.*, **45**, 2786–2794 (2018). https://doi.org/10.1002/2017GL076929
46. Hersbach, H., Bell, B., Berrisford, P. & Et al. The ERA5 global reanalysis. *Q. J. R. Meteorol. Soc.* **146**, 1999–2049 (2020). https://doi.org/10.1002/qj.3803
47. Rayner, N.A., Parker, D.E., Horton, E.B., Folland, C.K., Alexander, L.P., Kent, E.C. & Kaplan, A. Global analyses of sea surface temperature, sea ice, and night marine air temperature since the late nineteenth century. *J. Geophys. Res. Atmos.* **108 (D14)**, 4407 (2003). https://doi.org/doi:10.1029/2002JD002670
48. Eliassen, A., & Palm, T. On the transfer of energy in stationary mountain waves. Geofysiske publikasjoner **22**, 1–23 (1960).
49. Andrews, D.G., Mahlman, J.D. & Sinclair, R.W. Eliassen- Palm diagnostics of wave-mean flow interaction in the GFDL "SKYHI" general circulation model. *J. Atmos. Sci.* **40**, 2768–2784 (1983). https://doi.org/10.1175/1520-0469(1983)040<2768:ETWATM>2.0.CO;2
50. Jucker, M. Scaling of Eliassen-Palm flux vectors. *Atmos. Sci. Lett.* **22**, e1020 (2021). https://doi.org/10.1002/asl.1020
51. Du, W., & Hitchman M.H., Monthly mean Eliassen-Palm fluxes and EP flux divergences for boreal winter months (Dec-Jan-Feb) from 1979 to 2020 using ERA5 data (Data set). Zenodo (2023). https://doi.org/10.5281/zenodo.10140775

Figure captions

Figure 1. **QBO representation in EOF phase space** (a) Vertical profiles of EOF1 (solid line) and EOF2 (dashed line). (b) Scatter plots in the *PC1−PC2* phase space for boreal winter months (DJF). Dots represent neutral (black), El Niño (red), and La Niña (blue) periods. The numbers of months for these periods are written at the top right corner with same color. The centroid of all the points is shown with a green + marker. The QBO phase angle is defined to be $\theta = tan^{-1}\frac{PC2_C}{PC1_C}$, and $PC1_C$ and $PC2_C$ are defined with respect to the centroid point. Two data sample groups (G1 and G2) with opposite QBO phase are introduced for the central angle θ_c and half width $\Delta\theta/2$ (= ±60°). An example of G1 (pink circle arc) and G2 (light green arc) are shown for the central angle θ_c = 180°. (c) Composite mean of the zonal mean zonal wind for G1 (pink) and G2 (light green) groups at θ_c = 180° with ± one standard deviations. The dashed profile shows the composite difference G1 – G2, with circles on the right-hand side of the frame indicating a statistically significant result (> 95%) in the composite difference at the corresponding pressure levels. (d) Time variation of the QBO phase angle θ, where all months that are not DJF are shown with gray dots.

Figure 2. **QBO phase angle versus latitude plots of composite difference G1–G2 for DJF for the following zonal mean quantities**: (a–d) 100 hPa geopotential height anomalies (GPH′), (e–h) mean sea level pressure anomalies (MSLP′), and (i–l) surface temperature (T′) anomalies at 2 m height. From left to right, columns represent All, Neutral, El Niño, and La Niña periods. Black dots indicate regions with composite differences greater than 95% statistical significance. The vertical dotted line indicates the central phase angle θ_c = 180°, with vertical dashed lines for $\theta_c \pm$ 60°. Note that G1 – G2 at θ_c = 180°, is representative of QBO W – QBO E phase at 70 hPa and the reverse phase at 20 hPa (Fig. 1c).

Figure 3. **Northern Hemisphere orthographic polar projections (0°N–90°N) of** (a) 100 hPa GPH, (b) MSLP, (c) T at 2 m, and (d) snow depth at the central angle θ_c = 180° for neutral ENSO period during DJF. The 1st, 2nd, 3rd and 4th columns of each row represent the DJF climatological mean, composites of G1 anomalies (QBO W [E] at 70hPa [20hPa]), G2 anomalies (QBO E [W] at 70 hPa [20hPa]), and their composite difference G1–G2 (QBO W [E]–E [W] at 70hPa [20hPa]), respectively. Black dots on the composite difference plots highlight regions where statistical significance exceeds 95%.

590 **Figure 4. Regional anomalies (blue x's) of MSLP′ (top) and T′ at 2 m (bottom) as a function of QBO phase**
591 **angle for statistically significant domains observed in non-zonal composite difference analysis at θ_c = 180° over**
592 (a) the Polar region, (b) Southwestern Europe, (c) Eurasia and (d) North America, during DJF and for neutral ENSO
593 period. A sine trigonometric function with phase constant 90° is plotted as a black dashed line. Both opposite groups
594 G1 and G2 at θ_c = 180° are highlighted with a white color background, while the transition phases between these two
595 groups is highlighted with a light gray color background. The central vertical dotted line in each group G1 and G2
596 represents the central phase angle position of that group (i.e., θ_c = 180° for G1 and θ_c = 360° for G2), while the other
597 two dotted vertical lines represent the boundaries of that group ($\theta_c \pm \frac{\Delta\theta}{2}$, $\Delta\theta$ =120°, i.e., G1 ranges 120° - 240° and
598 G2 ranges 300° - 60°). The horizonal black solid line denotes the mean value of all the data points within that group.
599 One cycle of the QBO phase angle is plotted beginning at 60° so that both G1 and G2 are shown uninterrupted. The
600 bootstrapping between G1 and G2 for each panel is shown with adjacent histogram plots at the right-hand side, with
601 total 10, 000 resample size. The first histogram is for non parametric bootstrapping on the ratio of variance (f-test)
602 for G1 and G2 and the second is for bootstrapping on the difference of the mean for G1 and G2. The region inside
603 the two red vertical lines is at the 99% significant level.

604 **Figure 5**. **Latitude pressure sections of EP fluxes and EP flux divergence (color bar, m s^{-1} day^{-1})** (a) neutral, (b)
605 El Niño, and (c) La Niña, for the DJF climatological mean (1st column), QBO phase group G1 (2nd column), QBO
606 phase group G2 (3rd column), and G1 - G2 (4th column). G1(G2) corresponds approximately to QBO-W (E) at 70
607 hPa. EP flux arrows are scaled by $\sqrt{p_o/p}$ in order to see features in the upper stratosphere. Reference vector lengths
608 correspond to 10^6 kg s^{-2} (vertical) and $4x10^8$ kg s^{-2} (meridional) at 1000 hPa. Black, red and blue lines in the 1st, 2nd
609 and 3rd columns, respectively, are the zero-wind lines for zonal mean zonal wind for mean, G1, and G2, respectively.
610 The vertical solid line in each plot denotes the position of the equator. Black arrows on the composite difference plots
611 highlight regions where statistical significance exceeds 95%.

612 **Figure 6**. **Northern Hemisphere orthographic polar projections (0°N–90°N) of wind speed at 300 hPa at the**
613 **central angle θ_c = 180° during DJF**. The 1st, 2nd, 3rd, and 4th columns of each row represent the DJF climatological
614 mean, composites of G1 anomalies, composites of G2 anomalies, and their composite difference G1 – G2, respec-
615 tively. From top to bottom, rows are for (a) Neutral, (b) El Niño, and (c) La Niña. Black dots on the composite
616 difference plots highlight the regions where statistical significance exceeds 95%.
617

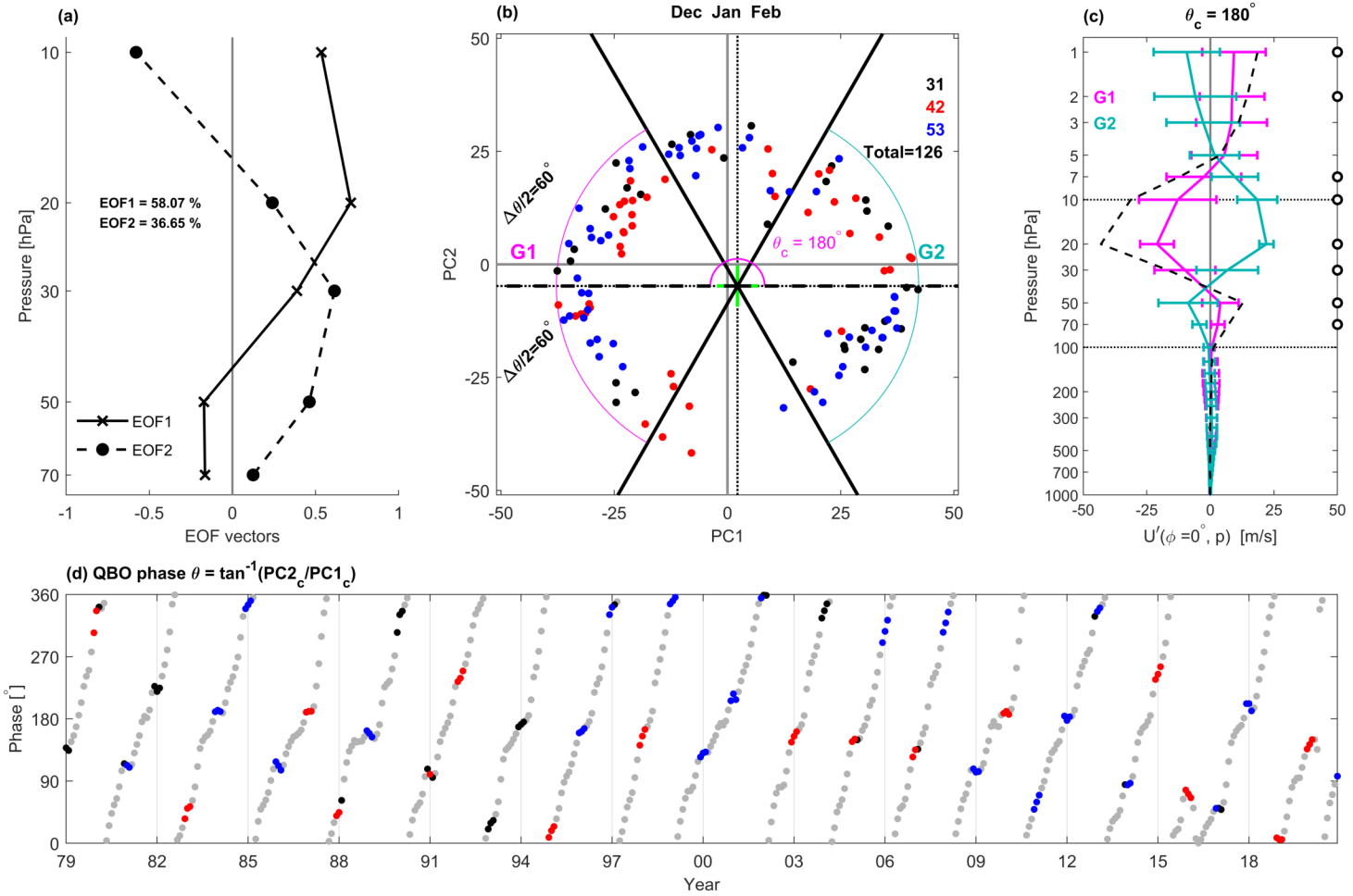
(a)
EOF1 = 58.07 %
EOF2 = 36.65 %
EOF1
EOF2
Pressure [hPa]
EOF vectors
(b)
Dec Jan Feb
31
42
53
Total=126
G1
G2
Δθ/2=60°
θc = 180°
PC1
PC2
(c)
θc = 180°
G1
G2
Pressure [hPa]
U′(ϕ =0°, p) [m/s]
(d) QBO phase θ = tan-1(PC2c/PC1c)
Phase [°]
Year

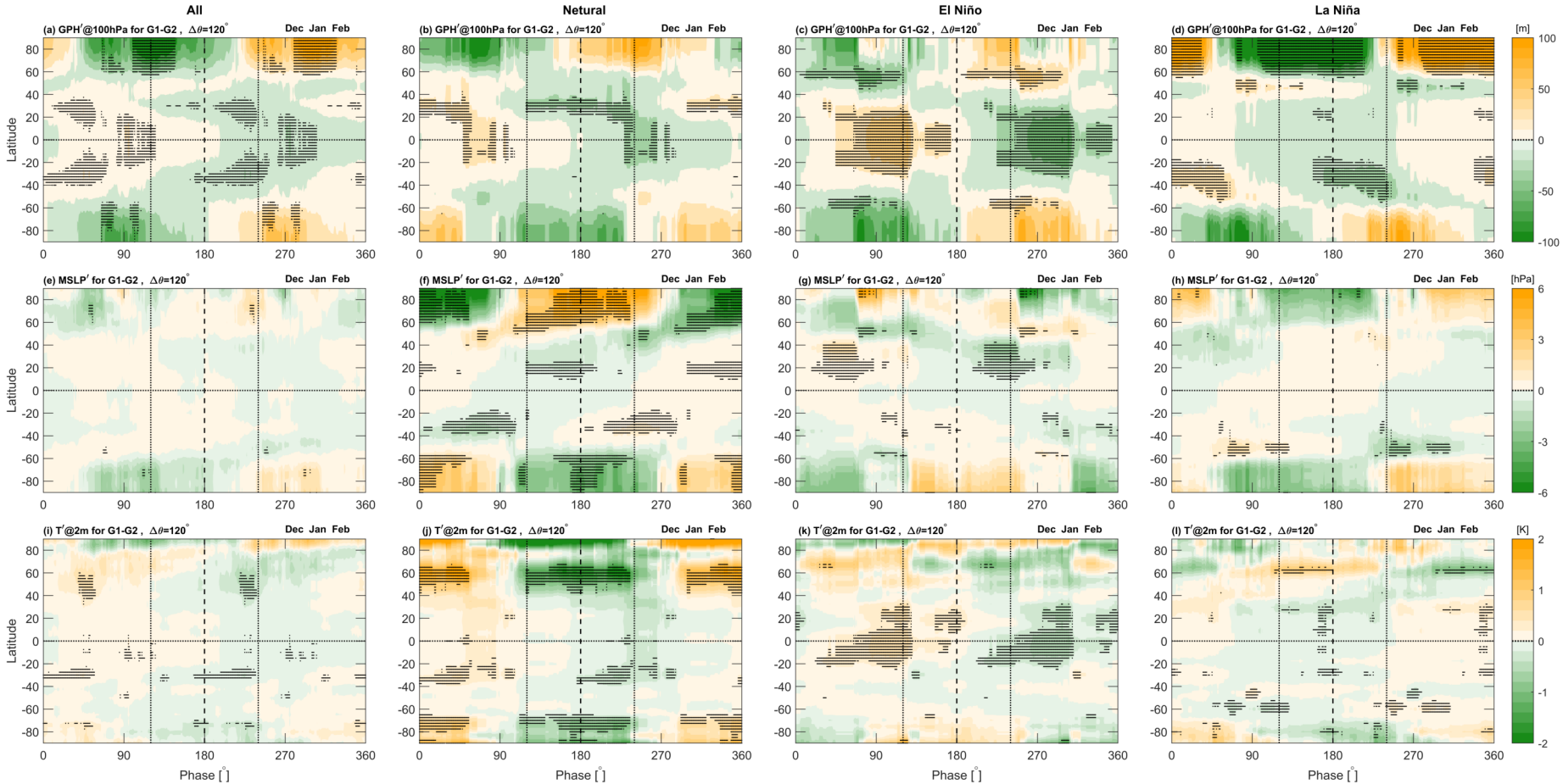
All
Netural
El Niño
La Niña
(a) GPH′@100hPa for G1-G2 , Δθ=120°
(b) GPH′@100hPa for G1-G2 , Δθ=120°
(c) GPH′@100hPa for G1-G2 , Δθ=120°
(d) GPH′@100hPa for G1-G2 , Δθ=120°
(e) MSLP′ for G1-G2 , Δθ=120°
(f) MSLP′ for G1-G2 , Δθ=120°
(g) MSLP′ for G1-G2 , Δθ=120°
(h) MSLP′ for G1-G2 , Δθ=120°
(i) T′@2m for G1-G2 , Δθ=120°
(j) T′@2m for G1-G2 , Δθ=120°
(k) T′@2m for G1-G2 , Δθ=120°
(l) T′@2m for G1-G2 , Δθ=120°
Dec Jan Feb
Latitude
Phase [°]
[m]
[hPa]
[K]

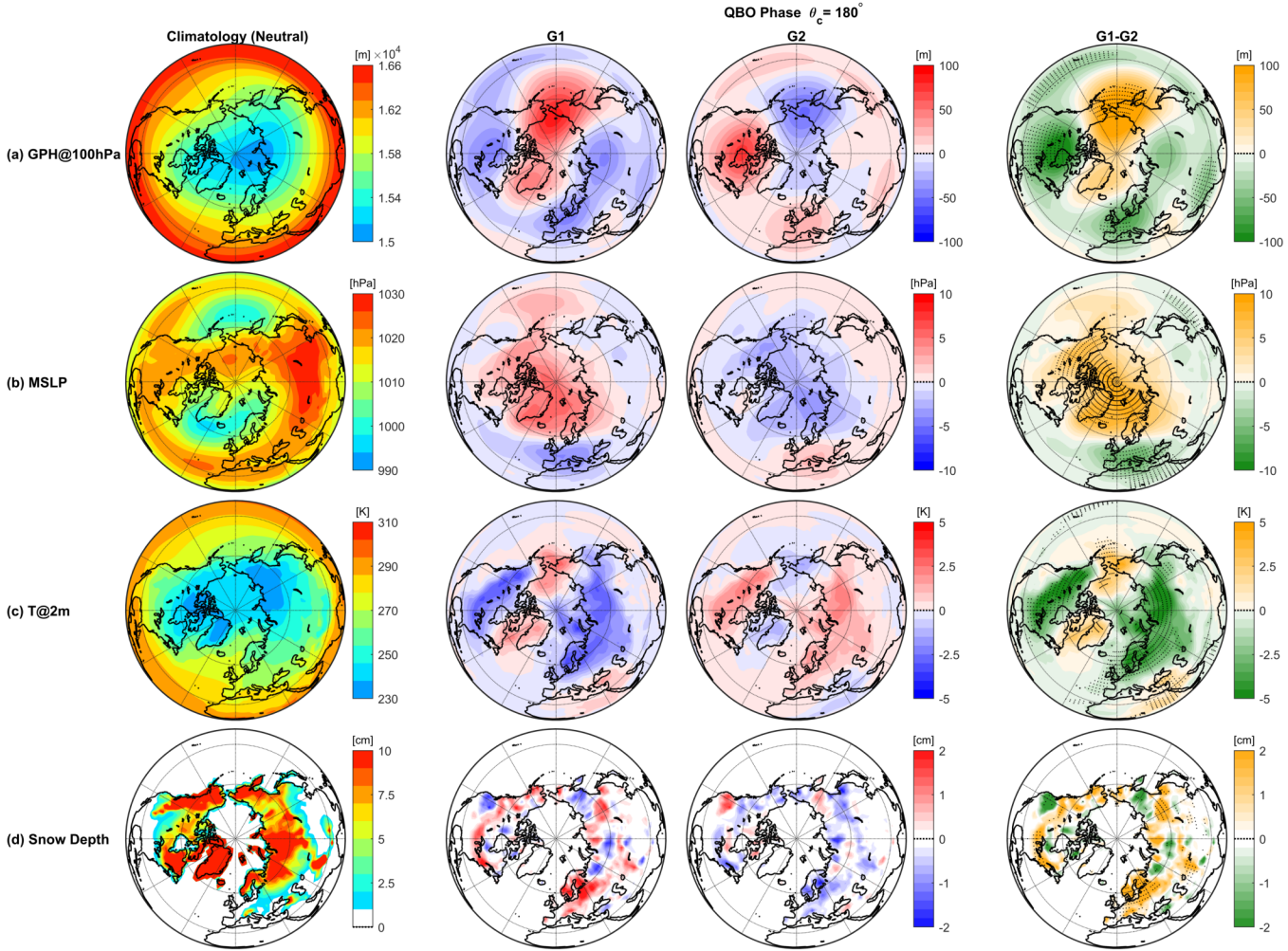
QBO Phase θ_c = 180°
Climatology (Neutral)
G1
G2
G1-G2
(a) GPH@100hPa
(b) MSLP
(c) T@2m
(d) Snow Depth
[m] ×10^4
1.66
1.62
1.58
1.54
1.5
[m]
100
50
0
-50
-100
[hPa]
1030
1020
1010
1000
990
10
5
0
-5
-10
[K]
310
290
270
250
230
5
2.5
0
-2.5
-5
[cm]
10
7.5
5
2.5
0
2
1
0
-1
-2

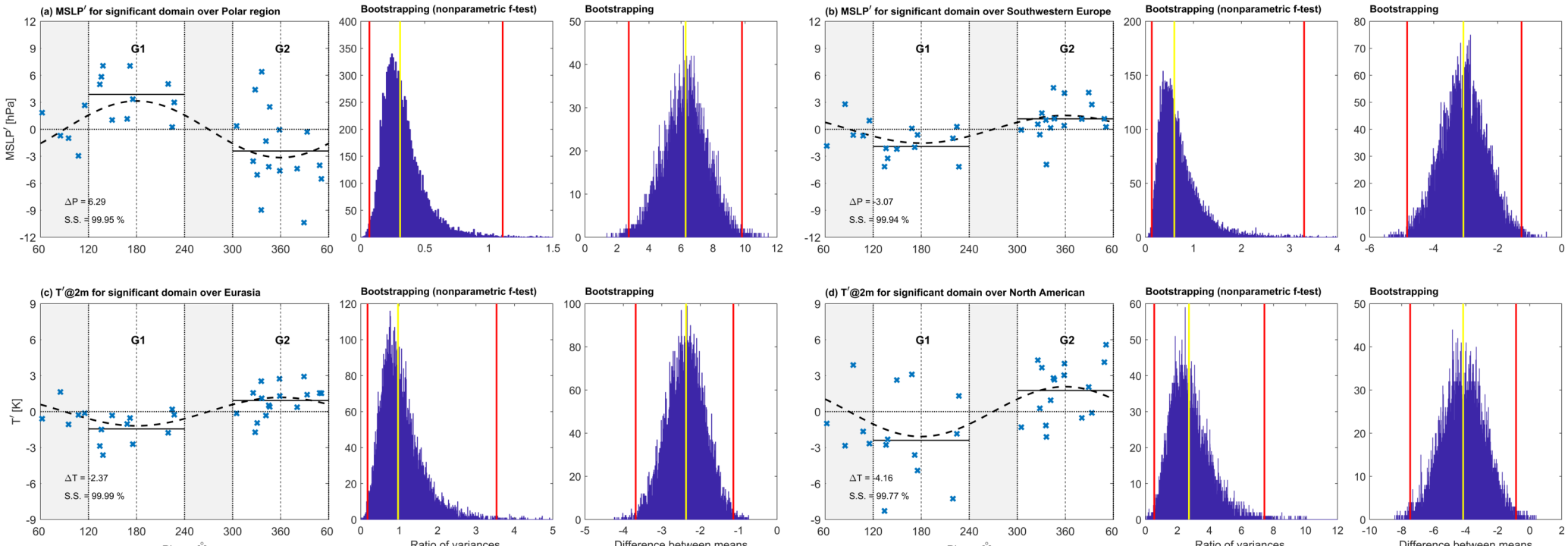
(a) MSLP′ for significant domain over Polar region
Bootstrapping (nonparametric f-test)
Bootstrapping
(b) MSLP′ for significant domain over Southwestern Europe
Bootstrapping (nonparametric f-test)
Bootstrapping
MSLP′ [hPa]
G1
G2
ΔP = 6.29
S.S. = 99.95 %
ΔP = -3.07
S.S. = 99.94 %
(c) T′@2m for significant domain over Eurasia
Bootstrapping (nonparametric f-test)
Bootstrapping
(d) T′@2m for significant domain over North American
Bootstrapping (nonparametric f-test)
Bootstrapping
T′ [K]
ΔT = -2.37
S.S. = 99.99 %
ΔT = -4.16
S.S. = 99.77 %
Phase [°]
Ratio of variances
Difference between means
Phase [°]
Ratio of variances
Difference between means

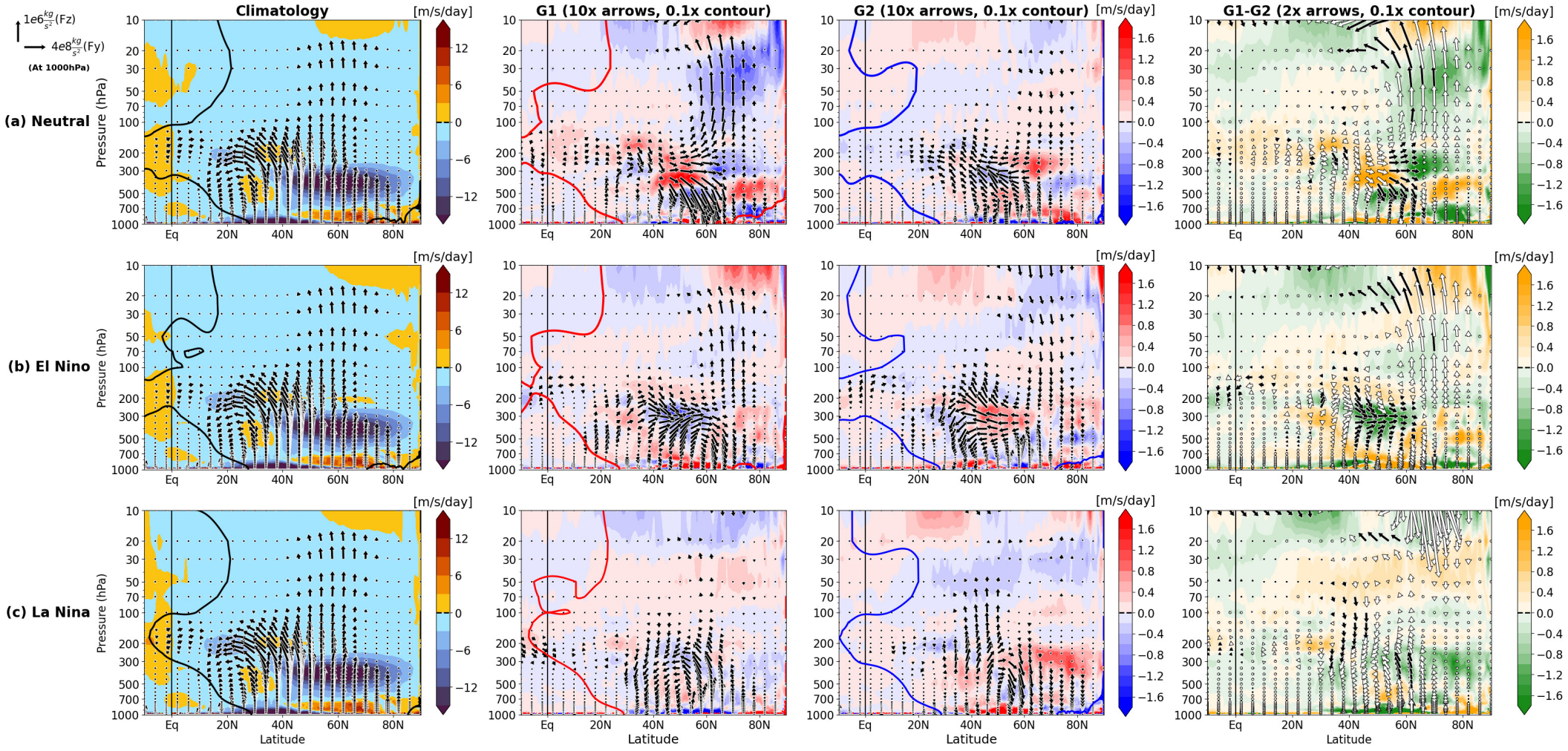
1e6 kg/s² (Fz)
4e8 kg/s² (Fy)
(At 1000hPa)
Climatology
G1 (10x arrows, 0.1x contour)
G2 (10x arrows, 0.1x contour)
G1-G2 (2x arrows, 0.1x contour)
[m/s/day]
(a) Neutral
(b) El Nino
(c) La Nina
Pressure (hPa)
Latitude
Eq
20N
40N
60N
80N

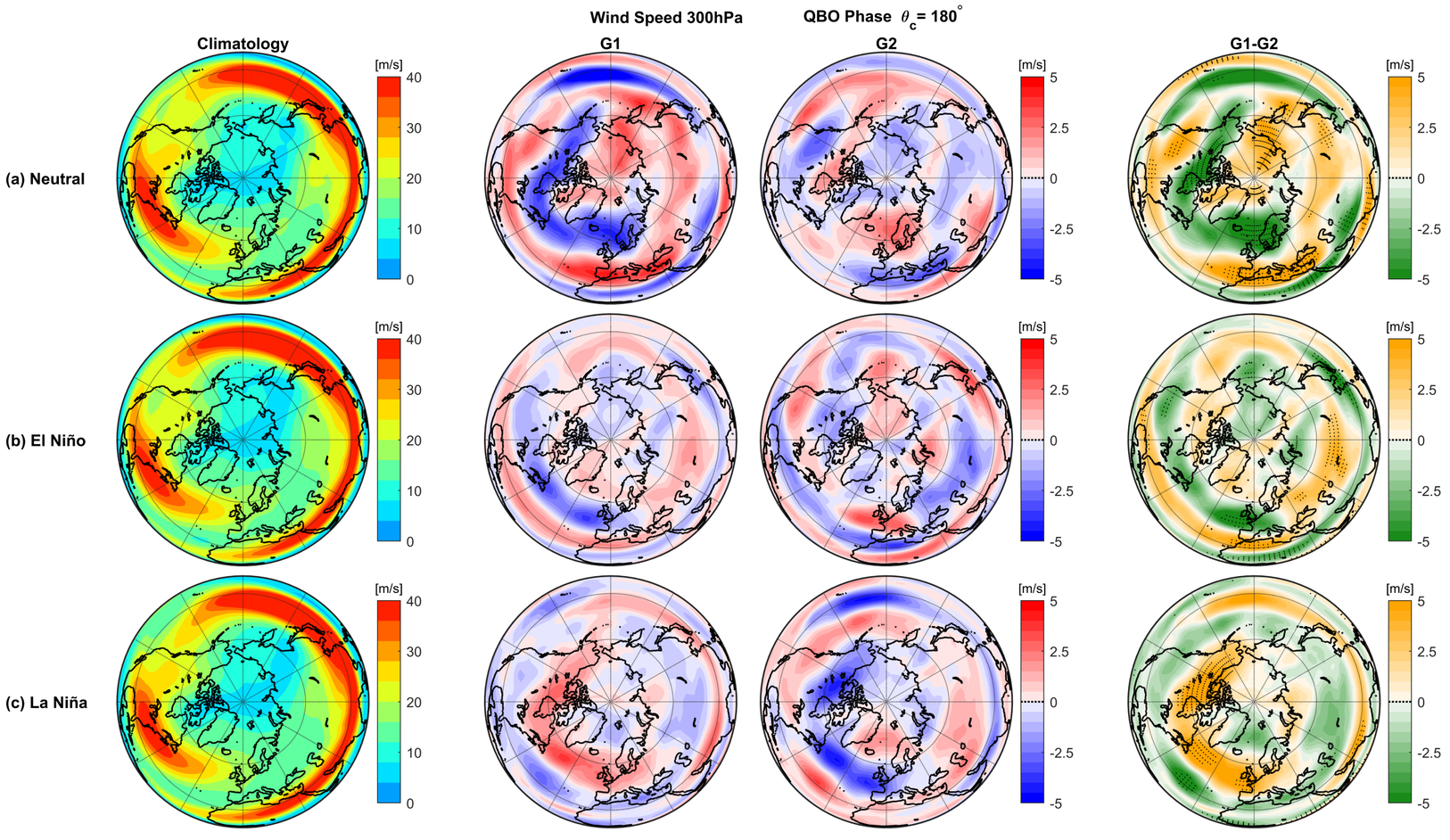
Wind Speed 300hPa
QBO Phase θ_c = 180°
Climatology
G1
G2
G1-G2
(a) Neutral
(b) El Niño
(c) La Niña
[m/s]
40
30
20
10
0
5
2.5
0
-2.5
-5